Efficient energy-dissipative bioinspired architectured composite materials with high mechanical properties

P.L. Pichard, L. Maheo, Justin Dirrenberger, M. Castro, U. Lafont, A. Le Duigou

Additive Manufacturing 109 (2025) 104875

Contents lists available at ScienceDirect

Additive Manufacturing

journal homepage: www.elsevier.com/locate/addma

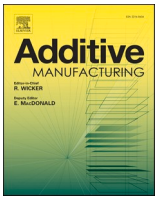

Efficient energy-dissipative bioinspired architectured composite materials with high mechanical properties

P.L. Pichard [a,*], L. Maheo [a,b], J. Dirrenberger [c,d], M. Castro [a], U. Lafont [e], A. Le Duigou [a,d]

[a] IRDL, Université de Bretagne Sud, UMR CNRS 6027, BIONICS Group, Lorient 56100, France
[b] CREC, Saint-Cyr-Coëtquidan, Guer 56380, France
[c] PIMM, Arts et Métiers, CNAM, UMR CNRS 8006, Paris 75013, France
[d] Institut Universitaire de France, Paris, France
[e] ESA, ESTEC, TEC-MSE, Noordwijk 2201 AZ, the Netherlands

ARTICLE INFO

Keywords:
Architectured materials
Bioinspired materials
Energy dissipation
Continuous filament fabrication

ABSTRACT

Additive manufacturing of stiff and strong architectured composite materials enables to replicate the intricate architectures found in biological systems while providing excellent mechanical performance, paving the way for efficient energy dissipative systems. By abstracting different Bouligand architectures found in various marine creatures, the innovative concept of pseudo-orthogonal Bouligand architectured laminates (POB) is introduced to address the requirements of energy dissipation. POB are also coupled with the introduction of functional voids, which geometry and content are inspired by the pore canals present in the exocuticle and endocuticle of the lobster shell. The different architectured laminates are 3D-printed with PolyAmide 12 (PA12) reinforced by continuous basalt fibre. Novel POBs concepts are tested under non-perforating low-velocity impact at 9.4 $m.s^{-1}$ and an impact energy of 50 J, along with more conventional stacking sequences to allow for comparison. All the tested samples dissipate at least 73 % of the impact energy, with porous POBs demonstrating the highest efficiency, ranging from 90 % to 95 %. This represents an improvement of up to 10 % compared to their denser counterparts, while also being 30 % lighter. The resulting performance in terms of energy dissipation capacity is then attributed to the underlying damage mechanisms imparted by the architecture, highlighting the desirable behaviour of porous structures.

1. Introduction

In aerospace and defense sectors, advanced structural materials are required to build durable aircrafts and spacecrafts in challenging environments, meeting demands of lightness, stiffness, strength and impact resistance. Space applications in particular face a broad spectrum of threats, from minor damage during maintenance to space debris and micrometeoroids [1,2]. Composite materials are prime candidates, but their energy dissipation capacity and damage tolerance may remain a weak point. The most straightforward strategy is to select materials with improved mechanical and physical properties. Another one consists in architecting the material, in other words to add a scale of order within the material to achieve what could not be obtained by the bulk material itself [3]. In this regard, living systems are an endless source of inspiration, as many of them need to protect themselves from various threats inherent to their environment. They rely on a very broad range of architectured materials [4–6] that can impart impact resistance and high energy-dissipation capacity, effectively balancing strength and toughness, which are generally paradoxical properties in bulk materials [7]. Such structures also aim at protecting vital organs during growing or at restraining the propagation of the impact effects to the entire biological system; they must therefore be able to alleviate the force, displacement, acceleration or transmitted energy. Although the materials used can largely vary from one biological system to another, all natural structures can be described with a eight features: fibrous, layered, helical, cellular, tubular, suture, overlapping and gradient [8].

When employing fibre-reinforced polymer composites, the first two design features are easy to meet. It is also possible to include a third one, namely the helical arrangement or Bouligand architecture. It can be defined as a laminate in which adjacent plies are rotated by a weak definite pitch angle testifying the natural slow growing process in the living systems. The generated helicoidal structure imparts in-plane

* Corresponding author.
E-mail address: pierre-louis.pichard@univ-ubs.fr (P.L. Pichard).

https://doi.org/10.1016/j.addma.2025.104875
Received 10 February 2025; Received in revised form 28 May 2025; Accepted 29 June 2025
Available online 30 June 2025

isotropy [8,9], and is encountered as a key feature in the dactyl club of the mantis shrimp [10], bone [11], fish scales [12,13], crustacean shells [14], but also as part of larger structures in the beetle elytra [15] or the cuttlebone [16]. Each ply is made of composite material with fibre bundles reinforcing a protein-based matrix [17], or even through a single structure [10]. More precisely, structures designed for impacts in the range of 20 $m.s^{-1}$, such as the dactyl club of the mantis shrimp, exhibit a property gradient through the thickness, with highly mineralized top layers and a decreasing pitch angle when moving to bottom layers [10].

The superior paradoxical toughness/stiffness behaviour of Bouligand structures (BS) under out-of-plane loading lies in the complex failure pattern which promotes subcritical damage and delays catastrophic failure, i.e. crack branching, fibre failure and delamination [10,18,19]. Modulating the ply orientation has become recurrent within bio-inspired BS [30,31], and more complex stacking sequences are proposed, such as the double-helicoidal configuration [20]. Low pitch angles promote twisting matrix cracks and diffused delamination, while larger angles favour fibre failure and large delamination areas [18,19]. The specificity of BS among crustaceans comes from the in-plane fibre arrangement, which is not straight, but forms a honeycomb-like structure forming a porous network [14,21,22]. A similar architecture was reported for crabs [23], both are more developed than that reported by Yaraghi and al. in the mantis shrimp appendage [24].

To account for the multifunctionality given by the tailored intricacy of natural structures, additive manufacturing is of growing interest in bio-inspired structures, and BS are no exception [25–29]. Indeed, this technology drastically simplifies the material deposition and thus enables to explore more complex geometries that would be tedious to manufacture with conventional processes. The continuous filament fabrication (CFF) is an additive manufacturing technology derived from the fused filament fabrication (FFF), where the thermoplastic polymer matrix of the filament is reinforced by continuous fibre reinforcement to produce high performance composite materials. Most of the reinforcements are carbon and glass fibres, but Kevlar, basalt and several plant fibres have already been employed to a lesser extent [30]. CFF is particularly suited for high performance bio-inspired BS, as natural systems often use fibre-reinforced composites [8].

Non-rectilinear arrangement and porous BS remain however little explored despite their potential. A thermoplastic 3D-printed lattice with helically oriented tubules tested in quasi-static compression revealed a transition between an auxetic behaviour and a global buckling [31]. A 3D-printed elastomeric lattice was also proposed and tested under quasi-static compressive loading, underlining the importance of the position of the centre rotation with respect to the filament spacing [28]. Indeed, this determines the alignment of intersection points in the lattice. It was also observed that the more the intersection points are scattered and the larger the pitch angle, the lower the stress within the lattice [28]. Moini and al. proposed a similar lattice, made of hardened cement paste, and observed that the porous interfaces enabled micro-cracking localization, thus enhancing the fracture resistance [25].

Yin and al. took advantage from the porosity inherent to the continuous filament fabrication, and concluded that superior energy absorption capacity is provided via pore collapsing, localized micro-cracking and formation a preferential path for twisting cracks [32]. Another study focused on in-plane pores forming tubules through the thickness of the laminate, highlighting that porous BS have a higher fracture strength due to damage accumulation in the vicinity of the pores compared to other ply stackings [33]. However, the properties of a porous Bouligand architecture are seldom combined with high performance composite materials to obtain stiff and tough structures. In addition, rigorous comparison with dense counterparts is still rarely proposed despite it remains a mandatory step to their development.

The challenge addressed is to develop composite structures which meet requirements of stiffness, strength, impact resistance and lightness. For that purpose, innovative pseudo-orthogonal Bouligand laminates are introduced and explored, bridging the gap between single and double Bouligand configurations reviewed in the previous paragraphs. A second part of the work focuses on the controlled implementation of functional voids within the structure by modulating the ply pattern, similar to natural systems, with a view to reduce the mass. Deeper insights are brought on how bioinspired architectures can modulate the energy dissipation property of composite materials when submitted to a low-velocity impact thanks to tailored damage mechanisms. The variation of the pitch angle, with five different stacking sequences, is first investigated with dense samples, then functional voids are introduced using rectilinear and sinusoidal abstraction approaches. The architectures are 3D-printed using a high-performance composite material made of polyamide 12 (PA12) reinforced with continuous basalt fibres. The bioinspired architectures are then tested under non-perforating low velocity impact, using a hemispherical impactor developing an impact energy of 50 J. Their energy dissipation behaviour is qualified on the post-mortem samples and whenever possible directly via high-speed images obtained during the impact and using μ-CT in situ characterization. Finally, the energy dissipation capacities of the different architectures are compared with each other and according to other metrics such as the backface displacement.

2. Materials and methods

2.1. Materials

The composite filament used here (supplied by Suprem SA, Switzerland) consists of continuous basalt fibres of 8–15 μm in diameter embedded in a PA12 matrix and is referred to as PA12-basalt filament in the rest of the paper. Basalt is selected for its mechanical properties similar to glass fibres [34] and for its potential to be used for out-of-Earth manufacturing, especially on the lunar surface [35,36]. On the other hand, PA12 could be used for packaging purposes and re-employed at the end of its life as a binder for the basalt fibres [37]. The composite material is not part of the bioinspiration approach as such. The average filament area, fibre volume fraction and porosity volume, all measured via SEM image analysis, are respectively 0.2080 ± 0.0046 mm, 55.0 ± 4.2 % and 1.4 ± 0.9 %. The latter is similar to that of other filaments for the continuous fabrication technology [38], while the fibre volume fraction slightly exceeds the range of 30–50 % usually reported in literature and commercially available [39,40]. The glass transition and melting temperatures of the filament were measured to be equal respectively to 44.9 ± 1.3°C and 178.3 ± 0.1°C (see Figure S1).

2.2. Additive manufacturing: hardware and software

The 3D printer used here is derived from a Prusa MK3S+ , following the work described in references [39,41], which allows a much more accurate control over the filament deposition, and thus enables to reach a process-induced porosity as low as about 2 %, compared to around 10 % for off-the-shelf CFF printers [41]. An in-house-manufactured flat-tip brass nozzle with an internal diameter of 1.0 mm was installed instead of the original 0.4 mm E3D V6 nozzle, as well as a two-duct fan shro[ud to replace the default printing fan shroud. The printer is placed in *a* thermally isolated enclosure, which is passively heated during printing and the printing volume reaches *a* threshold of 40–48°C in steady-state operation. A custom-designed independent air-cooling system maintains a maximum of 40°C within the electronic compartment, to avoid any electrical hazard.

The continuous nature of the filaments and above all the absence of cutting device in the printing head prevents the use of conventional FFF or even CFF slicers. The object must be designed in one single-stroke trajectory. As a result, the nozzle path is programmed directly thanks to a routine coded in a CAD software (Rhino7/Grasshopper, Robert McNeel & Associates). This routine also implements the manufacturing

parameters and provides the Gcode script which is directly sent to the 3D printer.

2.3. Sample preparation

The filament spool is stored 24 h at 45°C in the oven prior printing. The print duration per sample (up to 15 h in this work) is considered negligible regarding moisture absorption [42], the spool is kept at ambient conditions (temperature: 20 – 26°C, relative humidity: 40 – 60 %). The enclosure is pre-heated and the print is launched when the printing volume temperature has stabilized. The printing parameters are reported in Table 1. The printing speed is not a constant parameter for the whole part but is locally adjusted as a function of the nature of the trajectory. This precise control over the printing speed enables to print as accurately as possible the expected programmed trajectories. Distinction is made between straight and curved nozzle paths, with a supplementary differentiation between angles below and over 90°. The more acute the angle and the lower the printing speed. Respecting tolerances when printing curves with the CFF technology is indeed a limit already raised for various materials [43,44]. The slight variation in diameter thus highlights the challenge in the accurate deposition of continuous fibre-reinforced filaments when printing intricate geometries, especially for high fibre content. Nevertheless, the low standard deviations demonstrate a reproducible manufacturing process.

After printing, eventual support structures are carefully removed, then the samples are then stored in a dedicated enclosure at 23°C and 56 % RH prior mechanical testing. All the samples have a circular outer shape, as programmed in the Gcode. The diameter expected was 71.20 mm, while the theoretical thickness was 6.00 mm for LH = 0.200 mm. It is more difficult for porous configurations to respect these dimensions. Indeed, the radii of curvature at the end of each segment are less acute than the tight 180°-turns of the dense samples, which induces a shorter filament sliding when printing (visible on the rear side of dense POB, in Fig. 5a).

2.4. Sample geometry

All samples are cylinders (~70 mm in diameter) having a stacking sequence of 30 layers. The diameter is a trade-off between a sufficiently large testing area, a reasonable printing time for each sample given the high number of layers and the slow printing speed, and a sparing material utilization as the filament is not available in large quantities. The detailed slicing and structural parameters for each configuration are given in Table 2.

2.5. Sample characterization

The samples are weighted (Precision series, Fisherbrand) and their dimensions are measured with a micrometre (IP65, Mitutoyo) and via image analysis acquired with an optical microscope (VHX-7000, Keyence). The investigation of the internal damage is performed via high-resolution computer tomography (GE/Phoenix V|tome|xsv) on one sample of each configuration of interest. The voxel resolution of 36 μm is selected to fully capture the volume of the specimens, at the expense of the detection of potential cracks smaller than the chosen resolution [45].

Table 1
Printing parameters used for PA12-basalt.

Parameter	Value
Nozzle temperature (°C)	260
Bed temperature (°C)	90
Enclosure temperature (°C)	40–48
Printing speed (mm.s^{-1})	2.5 for straight trajectories 2.0 for low-angle (lower than 90°) curved trajectories 1.0 for acute-angle (90° and higher) curved trajectories
Cooling fan power (%)	25 for the three first layers 100 for the others

2.6. Low-velocity impact testing

Dynamic low-velocity impact testing is realised on a catapult device designed by Galpin and Grolleau [46]. The entire test set-up is depicted in Fig. 1. The samples are mounted prior testing in a circular flush-mounting with an effective testing area of 50 mm in diameter. The instrumented projectile used here is an aluminium cylinder equipped with an accelerometer, and strain gauges to record the impact force applied to the sensing projection end [47]. The tip of the projectile consists of a hemispherical steel impactor (13 mm in diameter, 1.128 kg for the total projectile mass). The projectile is flung via compressed air and guided along rails to the target (Fig. 1 A). The impact velocity is determined as a trade-off between two constraints. First, the perforation of the sample is not desired, as the scope of this study is to find the structure dissipating the highest amount of the impact energy, without reaching complete fracture. Secondly, the projectile should not collide with the sample top surface (i.e. the maximal displacement should not exceed the impactor length). Following preliminary adjustment tests, the target velocity is set to 9.4 ± 0.3 m.s^{-1} (i.e. an impact energy around 50 J), which matches those two constraints; the energy dissipation is then maximized for the configurations presenting the earliest rupture.

The result of the test is the evolution of the force as a function of the displacement. On the principle of redundancy, each of these two values are measured simultaneously twice by independent sensors. The force $F(t)$ is retrieved from the strain gauges, and from the accelerometer data using Newton's second law of motion (1).

$$F(t) = ma(t) \tag{1}$$

with m the projectile mass and a the acceleration. Considering that the projectile decelerates and moves downwards, and that the displacement is equal to zero at impact, the displacement of the projectile $u(t)$ is calculated as follows (2):

$$u(t) = \left(v_{impact} - a(t)dt\right)dt \tag{2}$$

The displacement is also retrieved from digital image correlation (VIC-2D, Correlated Solutions) via the following of a speckle pattern with a high-speed camera (FASTCAM Nova S12 type 1000K-M-16GB 10GbE, Photron), where images have a shutter speed of 1/50,000. A second identical camera films the backface of the sample (Fig. 1B). Data are recorded at 1 MHz for the accelerometer and the strain gauges, and 10 kHz for the images from the high-speed cameras.

The low-velocity impact test results are then analysed by means of a custom Python script. The area under the force-displacement curve equals to the energy dissipated by the sample – and not the energy absorbed, as none of the samples tested in the frame of this study were fully perforated, they all bounced back up. In the rest of the study, the force is retrieved from the strain gauges, and the displacement is calculated from the acceleration; the reason being that these sensors are respectively located nearer to the impact point, and more precise. The impact energy is calculated via the projectile velocity at impact. In order to compare the different energy dissipation potential of the various architecture material, an energy dissipation efficiency factor η is introduced as a performance index (3)(4). The higher η the more efficient the architecture considered at dissipating the energy of the impact.

$$\eta = \frac{E_{dissipated}}{E_{impact}} \tag{3}$$

with

Table 2
Laminate architectures and their associated structural parameters.

Sample reference	CP	QI	POB 93°	POB 96°	POB 102°	BPR 93°	BPS 93°
Sample overview		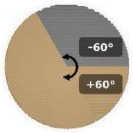		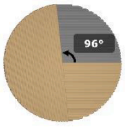	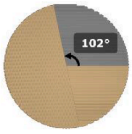	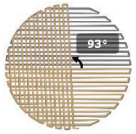	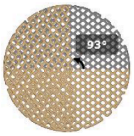
Complete naming	Cross-ply	Quasi-isotropic	Pseudo-orthogonal Bouligand with a 93° pitch angle	Pseudo-orthogonal Bouligand with a 96° pitch angle	Pseudo-orthogonal Bouligand with a 102° pitch angle	Pseudo-orthogonal Bouligand with a 93° pitch angle integrating a rectilinear pore pattern	Pseudo-orthogonal Bouligand with a 93° pitch angle integrating a sinusoidal pore pattern
Category	Widely-used laminate	Widely-used laminate	Dense POB	Dense POB	Dense POB	Porous POB	Porous POB
Density ($g.cm^{-3}$)	1.40 ± 0.02	1.46 ± 0.06	1.43 ± 0.05	1.45 ± 0.05	1.40 ± 0.04	0.93 ± 0.02	0.91 ± 0.01
Stacking sequence	$[0°/90°]_{15}$	$[0°/60°/-60°]_{5S}$	[0°/-87°/6°/-81°/12°/-75°/.../-6°]	[0°/-84°/12°/-72°/24°/-60°/.../-12°]	[0°/-78°/24°/-54°/48°/-30°/.../-24°]	Same as for POB 93°	Same as for POB 93°
Void content	Process-induced (<3%)	Process-induced (<3%)	Process-induced (<3%)	Process-induced (<3%)	Process-induced (<3%)	Theory: 30%	Theory: 30%
Pattern of functional voids	*NA*	*NA*	*NA*	*NA*	*NA*	Rectilinear	Sinusoidal

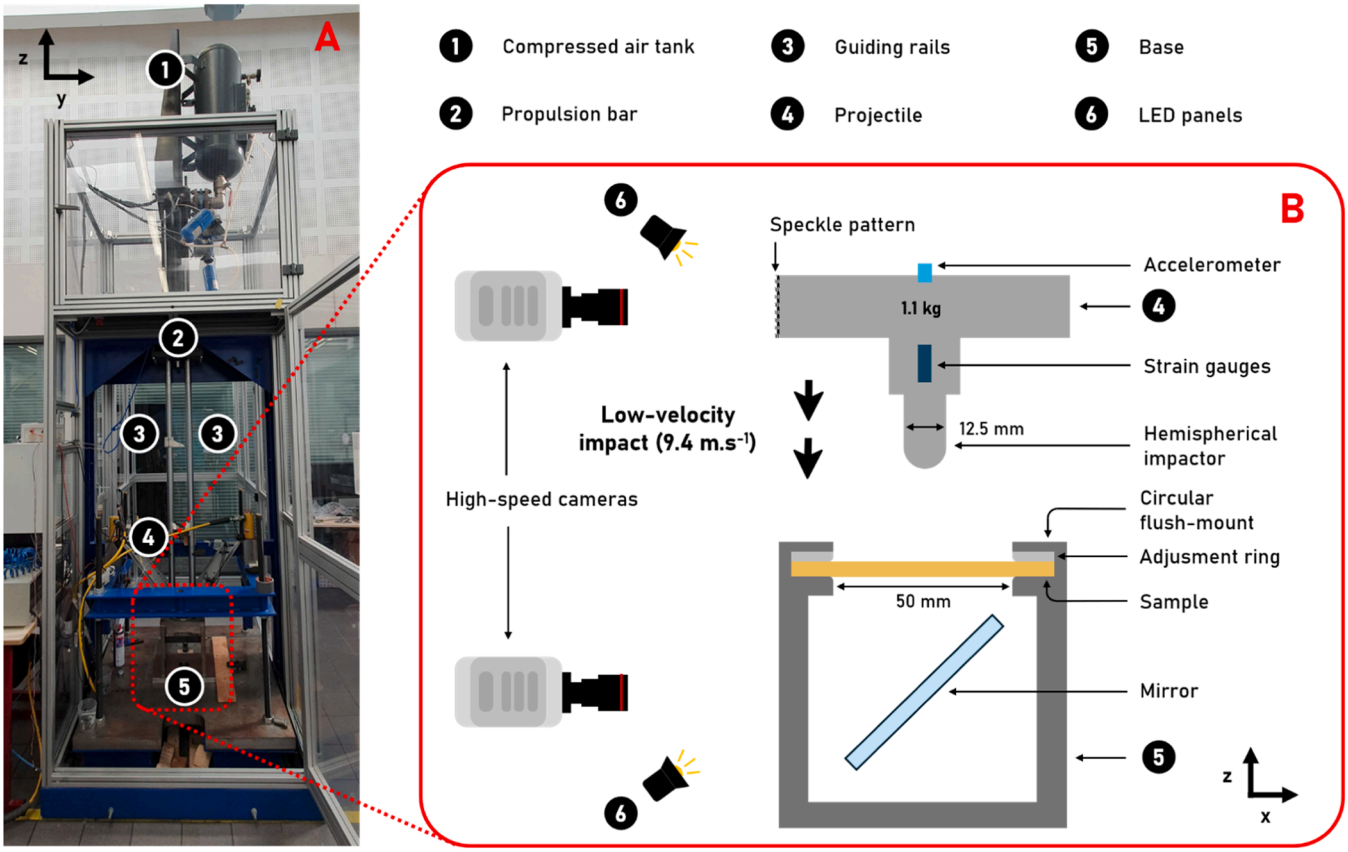

Fig. 1. Catapult testing device (A) - Detailed sample mount and data acquisition systems for low-velocity impact testing (B).

$$\begin{cases} E_{dissipated} = \int_0^{\Delta L_{residual}} F(\Delta L) d\Delta L \\ E_{impact} = \frac{1}{2} m {v_{impact}}^2 \end{cases} \quad (4)$$

The deformation of the rear side of the sample – opposite to the surface being hit by the projectile, referred to as front side – is also captured by a high-speed camera, for qualitative data analysis. A minimum of four samples per configuration were tested.

3. Results

3.1. Marine wildlife protection system microstructures as sources of inspiration for novel highly dissipative material with high mechanical properties

The pseudo-orthogonal Bouligand (POB) architecture proposed is inspired by the helical microstructures that can be found in the dactyl club of the mantis shrimp and in the scales of the coelacanth. It is indeed observed in single Bouligand structures that the smaller the pitch angle and the higher the energy dissipation capacity [18], [26]. In addition, double-helicoidal Bouligand configurations better withstand low-velocity impacts than single ones [20]. The POB stacking sequence is thereby a combination of single and double-helicoidal Bouligands (Fig. 2 G). As its name indicates, the pitch angle is 90 $+\alpha$, where α is the variable. The optimal pitch angle with regards to energy absorption or dissipation is found between 2.5° and 9.1° for single Bouligand structures [18,51], close to the range of 1.6° to 6° measured in the mantis shrimp appendage [10]. Double-helicoidal configurations show in turn better performance when the pitch angle is comprised between 9° and up to 20° [20,52]. Based on these results, it is expected that the POB structure presents an optimum of energy dissipation at low pitch angles, below 20°.

The layer number is fixed to 30 so that the overall laminate thickness remains reasonable; the pitch angle is set accordingly so that an integer number of complete rotations (180°) can be achieved. The calculation is slightly different from the other BS, as the orientation must be considered every two layers to take into account the pseudo-orthogonality of the structure proposed. Consequently, the 6° angle that should normally ensure the complete rotation in a single BS has to be halved. Hence the smallest tested angle is 93°. Angles of 96° and 102° respectively allow for two and four complete rotations through the sample thickness, staying in the range of promising pitch angles previously exposed (Fig. 2H).

Then, POB stacking sequence is combined with porous patterns abstracted from the pore canals that can be found in the exocuticles and endocuticles within the shells of various crustaceans, including lobsters (Fig. 2D) [14]. The pore canals take the form of a honeycomb-like network within the plane, where cells have an elliptical shape and are traversed by tubules that are both responsible for the transport of nutrients for shell mineralization and for vertical structural reinforcement [23]. Nevertheless, the effect of the pore canal geometry itself has not been investigated yet. Two infill patterns are designed here, defining the void geometry. The rectilinear pattern is a rough abstraction of the biological model, while the sinusoidal pattern shall replicate the more intricate morphology observed in the lobster exocuticle (Fig. 2I). The amplitude and spatial frequency are calculated so that voids respect an elliptical shape with a 3/1 ratio in length/width [53]. Porous samples present a programmed constant functional void content of 30 % in volume. The different configurations, their acronyms and detailed features are presented in Table 2.

3.2. Morphology of the 3D-printed architectures

Three different architecture strategies were abstracted: dense rectilinear (which corresponds to all widely-used laminates, POB 93°, POB 96° and POB 102° samples), porous rectilinear and porous sinusoidal (respectively corresponding to BPR 93° (pseudo-orthogonal Bouligand porous rectilinear) and BPS 93° (pseudo-orthogonal Bouligand porous

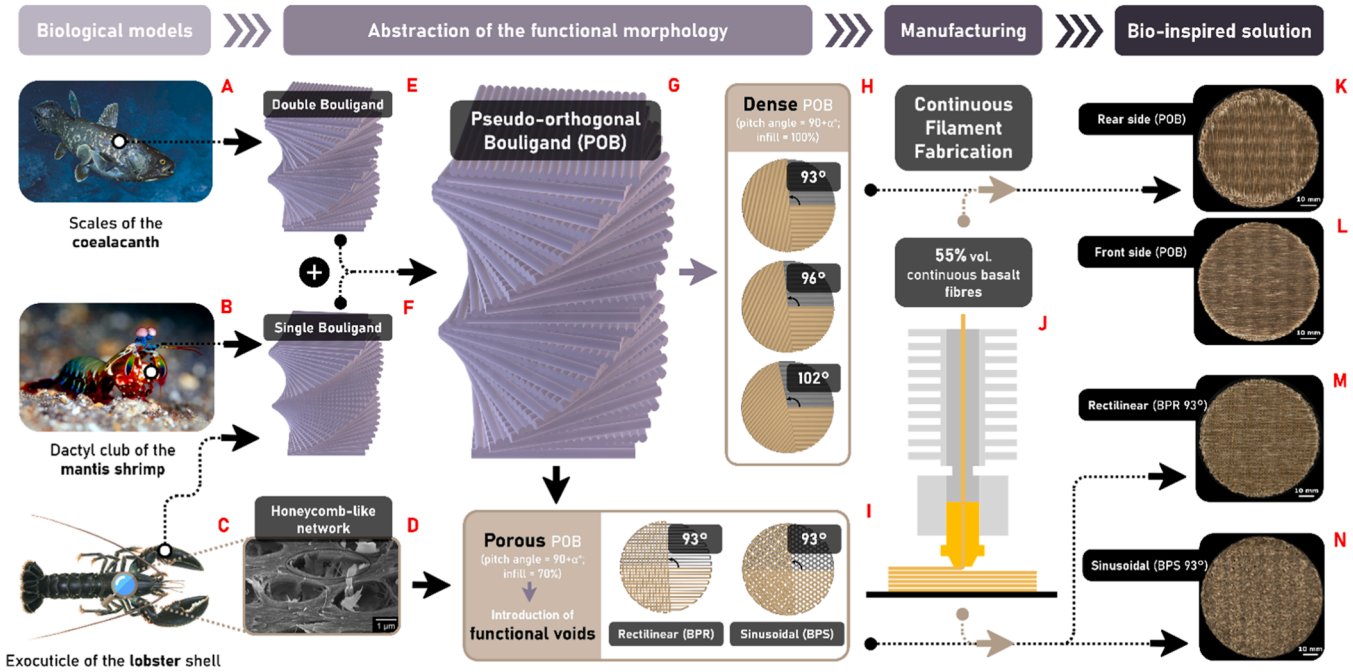

Fig. 2. Top-down biomimicry approach applied to the impact resistance issue. The pseudo-orthogonal Bouligand structure (POB) is inspired from the microstructures of the coelacanth scales (A)[48], of the mantis shrimp dactyl club (B)[49] and of the exocuticle of the lobster shell (C, D)[21,50]. The stacking sequence obtained is a mix of single and double-Bouligand structures (E, F, G). The parameters evaluated here are the pitch angle (93°, 96° and 102°, with a dense rectilinear infill pattern) (H) and the infill pattern (rectilinear (pseudo-orthogonal Bouligand Porous Rectilinear – BPR) and sinusoidal (pseudo-orthogonal Bouligand Porous Sinusoidal – BPS), 93° pitch angle and 70 % infill)(I). The different configurations are 3D-printed with high-performance composite material (J, K, L, M, N).

sinusoidal).

The density variation among dense samples is essentially attributed to heterogeneities on the edges of the samples, which are dependent on the stacking sequence. On a lesser extent, the stacking sequence itself modifies the thermal history of the material and may influence the formation of process-induced pores. Finally, slight density variations in the filament are also noticed. Nevertheless, being far from the edges (~10 mm) the impact zone is considered to be unaffected by the heterogeneities and thus similar for all dense samples. Dense samples also exhibit slight variations between the front and the rear sides (Fig. 2K-L). The front side refers to the surface hit by the projectile, but it actually corresponds to the side which was in contact with the printing bed. The front side is consequently smoother and presents a lower presence of defects, but only this layer is different from the others. On the other hand, the rear side did not benefit from the re-heating and flattening provided by the nozzle, hence the rough edges partially lifting out-of-plane (whiter areas). The core of the specimen, submitted to the impact, remains however homogeneous along its thickness (Fig. 3A).

Porous rectilinear POB are programmed by increasing the interfilament distance (ID) during the printing process compared to the dense structure. This is beneficial to the printing accuracy as the curvature radius is slightly less abrupt. On the other hand, the inhomogeneous nature of the composite filament, concealed when the filaments are adjacent, is here more highlighted as section variation along single paths and fibre waviness become visible (Fig. 2 M). It is still worth noticing that the overall parallel arrangement of adjacent filaments is respected. The clear geometrical pattern of the inner cross-section, given by the stacking sequence, is to be seen in Fig. 3B. The porous sinusoidal structure introduces an additional order of complexity by creating a three-dimensional network where connection pins are not only located at the interface of adjacent plies, as with the other porous architecture, but also within a ply at the extrema of each sinusoidal (Fig. 3C). The precise positioning of the connection pins is complex to control due to the freedom of movement allowed to the filament within the nozzle. Consequently, the inner architecture is less regular than BPR, and has a foamy-like structure, with a blend of open and close functional voids, imitating the pattern of the exocuticle of the lobster shell (Fig. 2N and Fig. 3C).

3.3. Tailoring the impact behaviour by the architecture

The different bioinspired configurations are tested under non-perforating low velocity impact, by means of a hemispherical impactor developing an impact energy of 50 J at a velocity in the range of 10 $m.s^{-1}$. Force and displacement are recorded simultaneously during the test. Fig. 4A presents the typical energy dissipation response of a dense POB. submitted to low-velocity impact. The first phase (points 0 to (i)) is non-linear, presenting a structural stiffening from a displacement of 2.5 – 3 mm, as indicated by the steeper load increase. A local fibre reorientation during impact, the geometrical non-linearity induced by the high deformations to which the sample is submitted [54] and the sample geometry itself could explain this phenomenon. A slight load drop can be noticed at 0.5 – 0.7 mm displacement (Fig. 4A-B).

It results from the propagation of the flexural waves through the sample after they have been reflected on the circular flush-mount (Supplementary Figure S3). The sudden stiffness reduction (points (i) to (ii)) following the initial load increase is associated to damage progression within the sample, such as delamination and fibre failure. The latter brings strong oscillations that were also reported elsewhere [54]. The stiffness reduction onset and extent vary according to the laminate stacking sequence. The peak force is recorded at point (ii) and may be followed by a slightly decreasing force plateau, also depending on the considered stacking sequence (not visible in the curve presented in Fig. 4). The maximum displacement is reached at point (iii), meaning that the projectile velocity is null, and thus that the entirety of the impact energy has been absorbed by the sample. When the projectile bounces back, the sample is progressively unloaded. The fraction of the impact energy which was stored elastically is then released, but a residual displacement (point (iv)) remains as irreversible deformation was also involved. This explains the hysteresis, and the area under the load-displacement curve corresponds to the energy dissipated by the sample. The viscous nature of the material is taken into account in the dissipated energy. For all the tested samples, the impact conditions did not lead to complete through-the-thickness penetration and the projectile bounced back in all cases.

The architecture of the sample clearly influences the response in terms of energy dissipation. Cross-ply laminates (CP) stand out from the other configurations with the lowest peak force (10.4 ± 0.3 N), the largest maximal displacement (8.8 ± 0.1 mm), and a smooth force signal. At the other end of the spectrum, quasi-isotropic laminates (QI) display the largest peak force (14.0 ± 0.3 N) but the lowest maximal displacement (7.3 ± 0.1 mm). The force signal becomes jagged from 4 mm displacement. These results are in line with previous studies comparing CP and QI, where the stiffer response of QI is attributed to higher bending stiffness and smoother ply transitions [55,56]. The inflection point observed in the 2.5 – 3.0 mm region for the quasi-isotropic and POB laminates is also present for cross-ply, but shifted towards a higher displacement of 4.0 – 4.5 mm.

As pseudo-orthogonal Bouligand (POB) configurations also correspond to a quasi-isotropic stacking sequence, their load-displacement curve resembles that of the QI laminate. While the initial part of the non-linear loading is identical for all samples, the larger the pitch angle

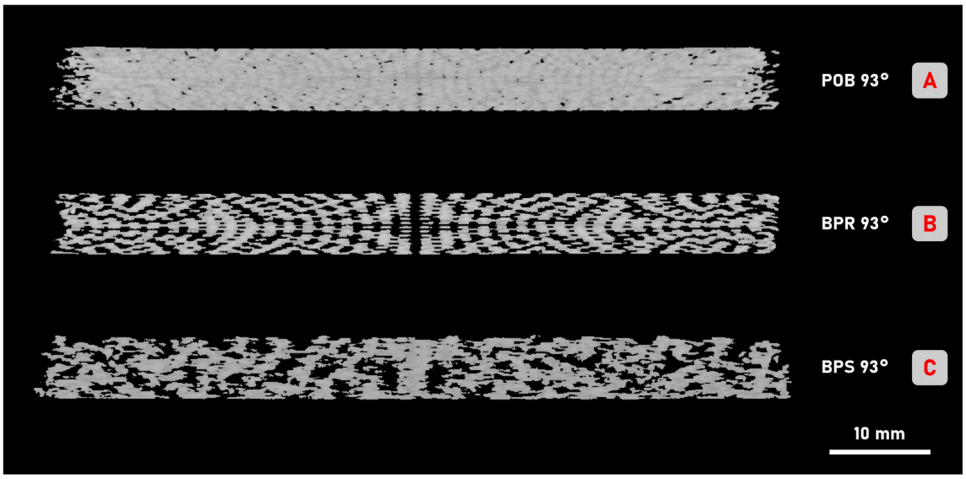

Fig. 3. Middle cross-sections of non-impacted POB 93° (A), BPR 93° (B) and BPS 93° (C) acquired via μ-CT-scan.

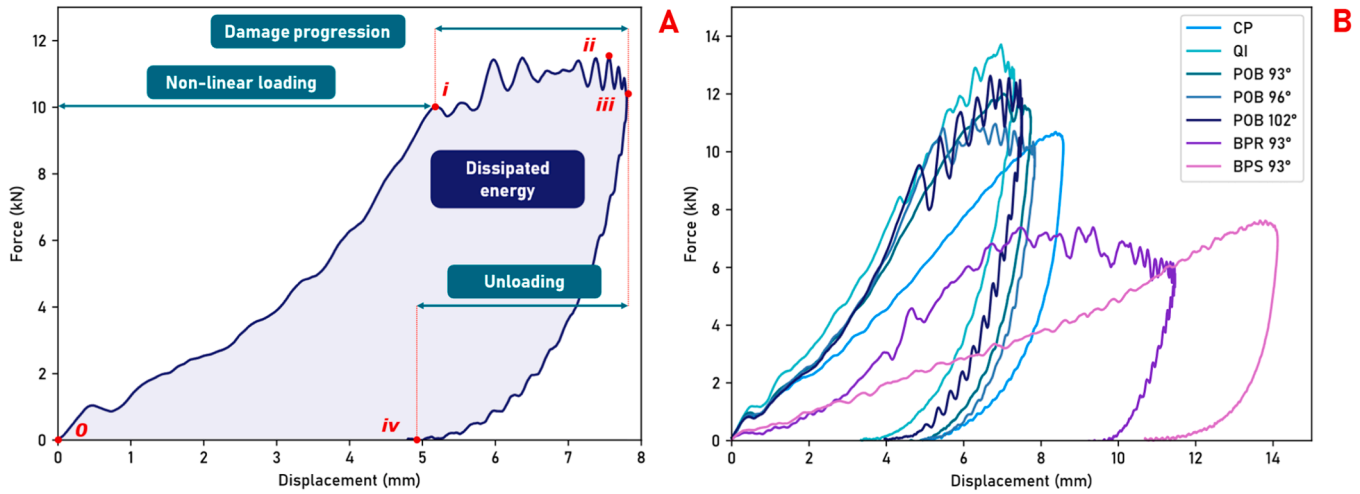

Fig. 4. (A) Typical force-displacement curve for a 50 J impact on a pseudo-orthogonal Bouligand (here POB 96°). (B) Representative force-displacement curves for all the configurations tested. All curves are provided in the supplementary Fig. S2. The different stacking sequences tested in dense samples are represented in shades of blue (CP, QI, POB 93°, POB 96° and POB 102°) while porous architectures are in purple (BPR 93°) and pink (BPS 93°).

and the higher the stiffening occurring after the inflexion point around 2.5 – 3 mm (Fig. 4B). This suggests that the impact response during the loading phase initially depends on the elastic properties of the material, before the architecture i.e. the material organization through the stacking sequence and the voids distribution, takes over. Nevertheless, while quasi-isotropic laminates (QI) do not show any change in the slope of the curve before peak force is reached, POB samples soften after an initial stiff response quasi-similar to QI, as shown in Fig. 4B. The onset of the slope discontinuity matches with the apparition of high amplitude oscillations in the force signal, except for POB 93° where this softening appears right before peak force and is followed by a force plateau. In fact, dense POB with a pitch angle of 102° have a similar impact response to single Bouligand laminates with a pitch angle of 12° [57]. The POB 93° shows the stiffest loading response, with a peak force reached at 11.9 ± 0.3 kN. The maximal displacement remains on the other hand fairly limited, to 7.8 ± 0.3 mm.

Unlike dense samples, porous samples do not show any clear initial artifact, indicating that wave propagation is notably different and likely dampened due to the reduced layer rigidity and the presence of numerous voids. BPR and BPS (respectively pseudo-orthogonal Bouligand porous rectilinear and sinusoidal structures), although containing the same content of functional voids, have dissimilar impact responses. The slope of the loading phase of BPR is much lower than that of the other dense samples, due to reduced in- and out-of-plane stiffnesses of the laminate introduced by the functional voids. This confirms the hypothesis that the first section of the loading part is more dependent on the material density while the subsequent stiffer section is governed by the architecture of the sample itself. As a matter of fact, the second section of the loading phase for BPR admits a stiffening slightly lower than that observed for POB 93°. Finally, all BPR samples present an almost constant force plateau between 6 and 7 kN, from 6.5 to 11.0 mm of displacement, the latter being the maximum reached by the projectile. Strong oscillations are visible from 4 mm displacement during the loading phase to the end of the force plateau, indicating that pore collapse, rupture of connection points between layers and fibre breakage occur simultaneously. This energy dissipation mechanism is similar to the elastic and plastic collapse phases of porous networks under low-velocity impact [58], and also resembles the behaviour of ceramic Bouligand structures infiltrated by polycarbonate resin [59]; although the samples presented in our study did not undergo complete failure.

Fig. 4B shows that the complex sinusoidal architecture presents the largest displacement to stop the projectile among all the structures tested, measured at 14.2 ± 0.2 mm. Moreover, the peak force reaches only 7.4 ± 0.2 kN, which is comparable to the one recorded for BPR, but largely lower than that of dense samples. The impact response of the pseudo-orthogonal Bouligand porous sinusoidal configuration (BPS) has a similar phase to that of cross-ply laminates, i.e. without any force plateau before unloading occurs. The inflection point is here reported around 9 mm displacement, with a slight and constant stiffening beyond this point, until maximal displacement is reached. The lack of important oscillations in the force signal throughout the entire impact stands for an energy dissipation mechanism which is not based on fibre failure but rather promotes subcritical damage propagation. It is finally worth noting that the linear section of the unloading curve is similar for all the configurations, dense and porous, suggesting that the unloading behaviour is largely driven by the elastic properties of the material itself i.e. PA12-continuous basalt fibre and in a lesser extent by the material's architecture.

3.4. *Driving the energy dissipation mechanisms by the architecture*

Adjusting the architecture enables to activate preferential damage mechanisms, some of which help delay catastrophic failure and thus increase the impact resistance. The three main damage modes of laminate composites come up in order to dissipate the 50 J impact: fibre breakage, matrix cracking and delamination. Both external visualization via optical microscopy images of the front and rear side, and internal visualization via CT-scans, are employed to assess the energy dissipation mechanisms.

External visualization shows a various range of damages which depend on the stacking sequence. The clearly visible white circular markings on the rear sides – a little less discernible on the front sides – result from the sample clamping within the circular flush-mount (Fig. 5 A). The rear sides of the laminates are bulged, but no apparent damage is noticed apart from slight white and fairly linear lines for a few samples.

Kink-banding is a damage mode appearing on the top and bottom surfaces of laminates, and characterized by thin and white lines of various lengths, from a few millimetres up to the whole radius of the laminate (Fig. 5A-(i),(ii)(iii)(v)). It results from bending and compression stresses that initially cause the matrix to shear, and then fibres to rotate and bend until failure upon exceeding the fibre compressive strength [60]. This localized bending and cracking of several single fibres introduce air pockets that scatter the incident light and thus make kink-bands appear clearer than the bronze-like colour of basalt fibres. Kink-banding is observed on all types of samples on the rear side,

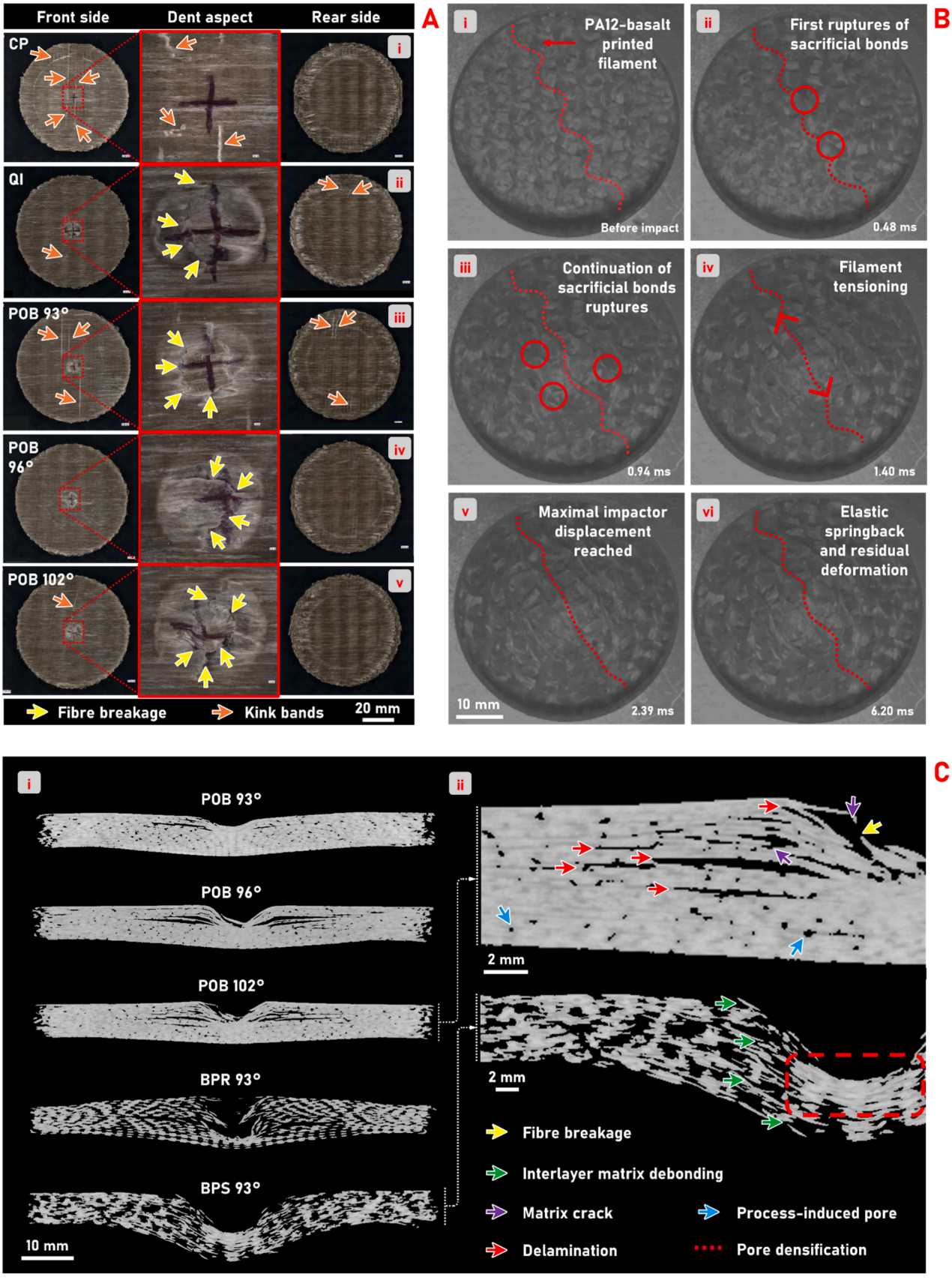

Fig. 5. (A) Post-mortem visualization of front and rear sides of the dense configurations (CP, QI, POB 93°, POB 96° and POB 102°)(i-vi) and close-up on the dent aspect on the front side. (B) High-speed image acquisition of the rear side of a porous sinusoidal sample during impact. (i): Non-impacted sample (as printed) – (ii-iv): Loading phase – (v): Maximal displacement reached – (vi): Sample after impact. (C) CT-scans of all the pseudo-orthogonal Bouligand configurations tested POB 93°, POB 96°, POB 102°, BPR 93° and BPS 93° (i) as well as identified specific damage mechanisms (ii).

although not on every test. It is located for the most part in the flush-mount area, and the kink band lengths do not exceed 15 mm. On the other hand, kink-banding systematically appears on the front sides of cross-ply laminates (CP) and POB 93° and only sometimes for POB 96°, POB 102° and quasi-isotropic laminates (QI). QI samples appear to be the less sensitive to this damage mode. These features are usually centered symmetrically on the point of impact and always follow the fibre orientation of the ply located right underneath (Fig. 5A-(i),(iii) – front sides). This suggests that kink bands originate from a matrix crack deeper in the laminate, and therefore that cross-plies and POB 93° dissipated a larger part of the impact energy via matrix cracking than the other configurations tested. Hazzard et al. also showed that cross-ply and helicoidal laminates are more prone to kink-banding than conventional quasi-isotropic laminates [56].

The rough edges of the indents clearly indicate fibre breakage (Fig. 5A-(ii),(v)), as compared to the smoother 1.5 mm indent for the lowest tested pitch angle. The deepest indentation marks are also the largest ones, with up to 12 mm of diameter for the QI and 11 mm for the POB 102° (Fig. 5A-(ii),(v)). The higher the pitch angle (and therefore the lower the fibre orientation mismatch between consecutive layers) and the more pronounced the dent mark, which means that cross-ply have the highest penetration resistance.

Inner insights of the damage that occurred during the impact are provided via CT-scans of the impacted samples, and complete the external visualization detailed previously. Cross-sections acquired at the impact location are presented in Fig. 5C-(i). The successive cross-sections of dense and porous Bouligand structures, from the impact location to 20 mm away from it, by step of 5 mm, can be found in the supplementary Figure S4. All dense POB configurations show similar damage modes that are comprised in a cylinder of 30–40 mm in diameter, although extent varies according to the pitch angle. At the point of impact, the projectile left a marked indent, as deep as 3 mm (half of the laminate thickness) for 96° and 102° samples.

The same damage modes are reported for POB 93°, POB 96° and POB 102°, which differ only in their extent. Large delamination areas are visible in all dense POB and are mainly located in the upper half of the laminate, extending symmetrically on either side beneath the point of impact (Fig. 5C-(i)), in a similar manner as single Bouligand laminates [45,61]. More specifically, the largest delamination area is located at the same height as the projectile dent depth. Delamination is qualitatively the lowest in POB 93° and is located at the interface of two layers, while it is more diffused through the thickness in POB 96° and 102°, in a similar fashion. Fibre breakage is also noticed deeper within the samples in the 96° and 102° configurations (Fig. 5C-(i) and yellow arrows of Fig. 5C-(ii)). This is in line with the strong oscillations recorded on the force signal as seen in Fig. 4B. Cracking is also suspected to occur within the filaments at the fibre/matrix interface, and not only at the filament/filament interface, although the characterization methods used did not allow direct observation. For all that, matrix cracking is hardly discernible given the resolution of the CT scanner that only shows cracks wider than 36 μm. Few matrix cracks are visible within the laminates and are mainly located at the interface of adjacent filaments (purple arrows of Fig. 5C-(ii)). The successive CT-scan slices do not reveal neither obvious helicoidal matrix cracks nor out-of-plane crack deviation (Supplementary Figure S4), as it could have been expected from the previous work on single Bouligand structures [19,25,62]. However, Yin and al. reported delamination instead of helicoidal matrix cracks as the major failure mode for their bio-inspired double-Bouligand configurations, which was linked to their enhanced energy absorption under low-velocity impact [20].

The rectilinear porous samples (BPR) show the highest delamination area among all the samples tested and scattered through the entire thickness. It is accompanied by extensive fibre breakage all along the edges of the indent (yellow arrows on Fig. 5C-(i)), explaining the ample and jagged oscillations during the loading phase and in the force plateau of the force-displacement curve (Fig. 4B). Slight material densification is also noticed at the tip of the indent mark, as evidenced by the whiter zone in Fig. 5C-(i).

The porous sinusoidal configuration (BPS) has a much different behaviour under impact than the other architectures presented here, and the only one for which the damage can be tracked over time and not only via post-mortem analysis. The printing trajectory is so conceived that two adjacent filaments within the same ply partially overlap at the extrema (maximum and minimum of each sinusoid), creating intra-ply connection points (Fig. 2I,N). They act as sacrificial bonds, giving way locally where the tensile stress exceeds the strength of the interface between the two overlapping filaments, while preserving the integrity of the remaining structure (Supplementary Video V1).

On the rear side, the first connection points to give way are those located in the immediate vicinity of the impactor axis, less than 0.5 ms after first contact between the impactor and the sample (red circles on Fig. 5B-(ii)). As the impactor moves downwards, the filaments located underneath the point of impact progressively stretch, leading to delamination and forcing more distant connection points to break in turn (Fig. 5B-(iii),(iv)). The filament tensioning is also accompanied by twisting along the fibre direction. The maximal displacement of the impactor is reached 2.39 ms after the impact, and the filament located at the apex of the sample is almost completely tightened (Fig. 5B-(v)). The fraction of the impact energy which has not been dissipated by the sample is returned to the projectile, causing it to bounce back. The unloading of the structure is thus ensured by the elastic springback of the sample. The whole impact duration, in case of sinusoidal samples, is around 6 ms. The damage mechanisms of BPS are thus matrix cracking and rupture at the matrix/filament interfaces, associated with localised delamination in the impact region as well as pore densification beneath the point of impact (Fig. 5B-(v),(vi)).

3.5. *Relative energy dissipation performance of architectured composite materials*

Fig. 6C represents the evolution of the energy within the sample, normalized by the impact energy, at any time of the impact. It can be noticed the initial energy absorption rate is similar for all the dense POB configurations as well as for quasi-isotropic laminates (QI). On the other hand, porous samples and to a lesser extent cross-ply laminates (CP) require much more time to both absorb impact energy. At point (i), the entirety of the impact energy is stored within the sample. The fraction should not in theory exceed 1, then the values beyond especially reflect the uncertainty associated with the force measurement, which has been shown to be subject to considerable oscillations in some architectures. At point (iv), the projectile is no more in contact with the sample and the impact duration can be determined; here, the shortest impact duration for a given architecture is represented. A fraction of the impact energy is returned to the projectile (arrow (ii)), which bounces back, whilst the rest is considered to be dissipated by the sample and corresponds to η (arrow (iii)). The impact duration greatly varies between the different architectures, with almost 8.1 ± 0.2 ms for BPS 93° while POB 93° requires only 3.0 ± 0.2 ms. More generally, the higher the maximal displacement recorded during the test and the longer the impact duration (Fig. 6A,B).

Plotting the energy dissipation efficiency factor η as a function of the maximal displacement measured during the impact (Fig. 6A) or as a function of the peak force (Fig. 6B) provides useful guidelines when it comes to design protective panels that, for a given thickness, have to offer high energy dissipation combined with high mechanical performance. For dense structures, the less visible the impact indent the higher the energy dissipation capacity of the laminate. As a consequence, a high mismatch of fibre orientation between adjacent layers is associated with high penetration resistance and superior energy dissipation. All the samples do dissipate a large part of the impact energy, with QI performing the worst with 75.1 ± 1.5 %. POB 93° present the best trade-off between a high energy dissipation capacity (84.7 ± 2.4 % of the impact

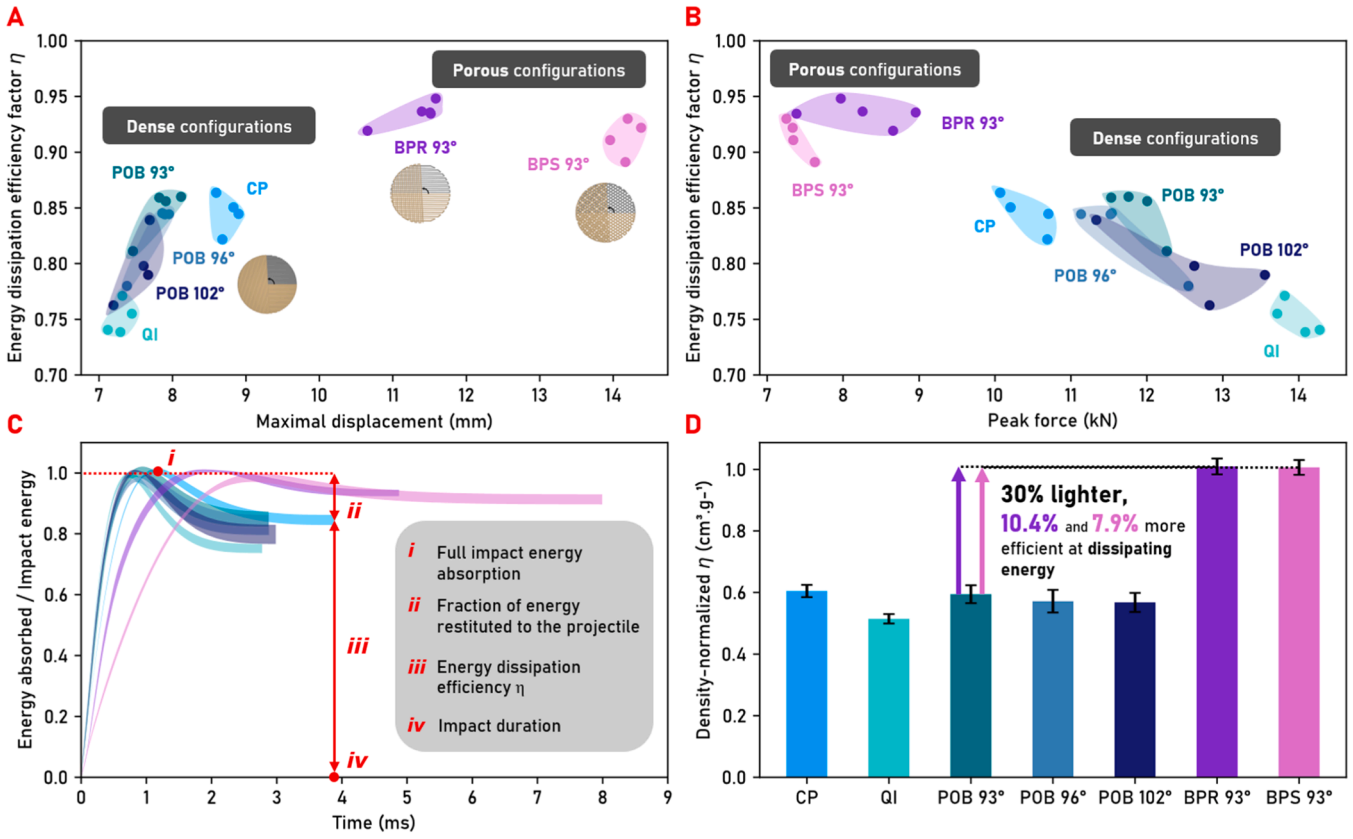

Fig. 6. Performance diagram of the energy dissipation efficiency factor as a function of the maximal displacement (A) and as a function of the peak force (B) – Evolution of the energy absorbed by the sample normalized by the impact energy. The width of each colour band corresponds to the standard deviation of all the samples tested for a given architecture (C) - Density-normalized energy dissipation efficiency factor (D).

energy), a moderate maximal displacement (7.83 ± 0.27 mm) and a moderate peak force (11.9 ± 0.3 kN). CP laminates dissipate the same amount of energy, but require more space to allow the panel displacement, which may be detrimental for backface protection.

Porous configurations are between 30 % and 35 % lighter than the dense samples, for a theoretical functional void content of 30 %. Consequently, the energy dissipation factor is divided by the density of the sample considered (Fig. 6B). Doing so further highlights the efficiency of implementing functional voids. The rectilinear and sinusoidal configurations are respectively 34.9 ± 3.6 % and 36.3 ± 3 % lighter than their dense counterparts but are yet able to dissipate between 8 % and 10 % more energy under the same impact conditions, which provides a density-normalized efficiency of up to 70 %. BPR demonstrates the highest energy dissipation capability among all the tested configurations, although this performance relies on the least desirable impact response as the main energy dissipation mechanisms identified are fibre fracture and delamination, associated with the deepest impact dent measured. With a similar energy dissipation efficiency and at the same density, BPS shows a completely different impact response, where the progressive breakage of the sacrificial connection points allows for the gradual tensioning of the filaments. The minor role of fibre fracture as damage mechanism indicates that the structural integrity of the material is preserved, and suggests a substantial potential for additional energy dissipation in case of multiple or stronger impacts.

4. Conclusions

In the context of novel impact-resistant materials for aerospace and defense applications, the top-down biomimicry approach developed here is successful in transposing natural Bouligand features found in different crustaceans into efficient energy-dissipative structural materials. The configurations proposed in the framework of this study demonstrate the relevance of the continuous filament fabrication technology to produce composites combining high energy dissipation with high mechanical performance, enabling to architecture the structure right down into the ply. This is particularly valid for the porous sinusoidal structures, which aim at replicating the in-plane intricate honeycomb-like pattern found within the lobster shells.

It is demonstrated that the pseudo-orthogonal Bouligand structures offer the possibility of reconciling in-plane isotropy, which is often required for parts submitted to complex loading cases, and enhanced impact resistance. More specifically, the smallest pitch angle of 93° provides the same energy dissipation capacity as a conventional cross-ply laminates, i.e. around 85 % in the present test configuration, at the cost of a reduced peak force. Increasing the pitch angle enables to find a trade-off between a lower energy dissipation capacity, but a lower backface displacement and a higher peak force, i.e. imparting a higher stiffness.

The more intricate porous configurations are the highest energy-dissipative structures tested, with 91.4 % and 93.5 % of the impact energy dissipated respectively by BPS (sinusoidal) and BPR (rectilinear) samples. In comparison with their denser counterpart with the same pitch angle (POB 93°), the porous configurations are up to 10 % more efficient at dissipating energy, while being 30 % lighter. This means that a higher performance in terms of energy dissipation is reached with a lower number of resources, paving the way for lighter structures with reduced material consumption. The damage mechanisms revealed for BPR and BPS are however completely different to reach this performance. The sinusoidal configuration is the bio-inspired pattern closest to the lobster shell, and seemingly appears to be the most complicated to manufacture in a reproducible manner. It also exhibits the largest maximal displacement among all the structures tested, which is justly

detrimental to backface protection. Nonetheless, it also provides the most desirable damage configuration by the propagation of subcritical damage via localized inter- and intralayer filament debonding and progressive tensioning of the basalt fibres, preventing catastrophic fibre failure. In contrast, BPR energy dissipation is essentially ensured by fibre breakage during the impactor penetration and delamination, which are not controlled and may compromise the integrity of the entire structure.

The results presented here offer promising perspectives regarding bio-inspired structural materials that could withstand higher-velocity impacts, or even multiple impacts. Sharper projectiles could be employed for a better representativity of real-life application cases, such as hail, birds, or even space debris and micrometeoroids. Larger-scale structures can also be conveniently considered, with pseudo-orthogonal Bouligand that likely call for particular attention when stacking the plies but remain largely accessible with the conventional composite manufacturing processes and could thus be used in a near future. Porous configurations conversely require a much more advanced manufacturing process, as the latter must go down to the scale of the fibre instead of the ply. BPR and BPS could then be produced via AFP or ATL, the industrial equivalents of the CFF process used in this study.

Further work could involve the study of pseudo-orthogonal Bouligand porous samples with different pitch angles, such as what was performed in this study with the dense configurations. Additionally, the influence of geometric parameters on the energy dissipation of porous structures could be investigated as well, by varying for example the infill density or the pore shape.

CRediT authorship contribution statement

PL Pichard: Conceptualization, Data curation, Formal analysis, Investigation, Methodology, Writing – original draft. **L Maheo:** Conceptualization, Formal analysis, Methodology, Supervision, Writing – review and editing. **J Dirrenberger:** Conceptualization, Formal analysis, Methodology, Supervision, Writing – review and editing. **M Castro:** Formal analysis, Methodology, Writing – review and editing. **U Lafont:** Conceptualization, Funding acquisition, Resources, Supervision, Writing – review and editing. **A Le Duigou:** Conceptualization, Formal analysis, Methodology, Project administration, Supervision, Writing – review and editing.

Declaration of Competing Interest

The authors declare that they have no known competing financial interests or personal relationships that could have appeared to influence the work reported in this paper.

Acknowledgments

The authors wish to thank the Institut Carnot ARTS and the European Space Agency (contract numbre: 4000139402/22/NL/PA/pbe) for the financial support and Rodolphe HENRI from Suprem SA, Switzerland, for the supply of the PA12-basalt filament. Anthony JEGAT, Hervé BELLEGOU, Antoine KERVOELEN and Bertrand GALPIN from the Université de Bretagne Sud are also acknowledged for the technical support provided for the material characterization and the low-velocity impact testing. Alexis TOUPIN and Sabine RAGUENES are acknowledged for the obtention of μ-CT scans.

Author Agreement Statement

We the undersigned declare that this manuscript is original, has not been published before and is not currently being considered for publication elsewhere.

We confirm that the manuscript has been read and approved by all named authors and that there are no other persons who satisfied the criteria for authorship but are not listed. We further confirm that the order of authors listed in the manuscript has been approved by all of us.

We understand that the Corresponding Author is the sole contact for the Editorial process. He is responsible for communicating with the other authors about progress, submissions of revisions and final approval of proofs.

Appendix A. Supporting information

Supplementary data associated with this article can be found in the online version at doi:10.1016/j.addma.2025.104875.

Data Availability

Data will be made available on request.

References

[1] A. Lemartinel, M. Castro, O. Fouche, J.C. De Luca, J.F. Feller, Impact and strain monitoring in glass fiber reinforced epoxy laminates with embedded quantum resistive sensors (QRSs), Compos. Sci. Technol. 221 (2022) 109352, https://doi.org/10.1016/j.compscitech.2022.109352.
[2] V. Vanzani, F. Marzari, and F. Dotto, Micrometeoroid impacts on the lunar surface, 1997.
[3] M. Ashby, Designing architectured materials, Scr. Mater. 68 (1) (2013) 4–7, https://doi.org/10.1016/j.scriptamat.2012.04.033.
[4] M.K. Islam, P.J. Hazell, J.P. Escobedo, H. Wang, Biomimetic armour design strategies for additive manufacturing: a review, Mater. Des. 205 (2021) 109730, https://doi.org/10.1016/j.matdes.2021.109730.
[5] A. Ghazlan, T. Ngo, P. Tan, Y.M. Xie, P. Tran, M. Donough, Inspiration from Nature's body armours – A review of biological and bioinspired composites, Compos. Part B Eng. 205 (2021) 108513, https://doi.org/10.1016/j.compositesb.2020.108513.
[6] S.H. Siddique, P.J. Hazell, H. Wang, J.P. Escobedo, A.A.H. Ameri, Lessons from nature: 3D printed bio-inspired porous structures for impact energy absorption – a review, Addit. Manuf. 58 (2022) 103051, https://doi.org/10.1016/j.addma.2022.103051.
[7] R.O. Ritchie, The conflicts between strength and toughness, Nat. Mater. 10 (11) (2011) 817–822, https://doi.org/10.1038/nmat3115.
[8] S.E. Naleway, M.M. Porter, J. McKittrick, M.A. Meyers, Structural design elements in biological materials: application to bioinspiration, Adv. Mater. 27 (37) (2015) 5455–5476, https://doi.org/10.1002/adma.201502403.
[9] M. Meo, F. Rizzo, M. Portus, F. Pinto, Bioinspired helicoidal composite structure featuring functionally graded variable ply pitch, Materials 14 (18) (2021) 5133, https://doi.org/10.3390/ma14185133.
[10] J.C. Weaver, et al., The stomatopod dactyl club: a formidable damage-tolerant biological hammer, Science 336 (6086) (2012) 1275–1280, https://doi.org/10.1126/science.1218764.
[11] M.M. Giraud-Guille, Twisted plywood architecture of collagen fibrils in human compact bone osteons, Calcif. Tissue Int. 42 (3) (1988) 167–180, https://doi.org/10.1007/BF02556330.
[12] H. Quan, W. Yang, E. Schaible, R.O. Ritchie, M.A. Meyers, Novel defense mechanisms in the armor of the scales of the 'Living Fossil' coelacanth fish, Adv. Funct. Mater. 28 (46) (Nov. 2018) 1804237, https://doi.org/10.1002/adfm.201804237.
[13] E.A. Zimmermann, et al., Mechanical adaptability of the Bouligand-type structure in natural dermal armour, Nat. Commun. 4 (1) (2013) 2634, https://doi.org/10.1038/ncomms3634.
[14] P. Romano, H. Fabritius, D. Raabe, "he exoskeleton of the lobster Homarus americanus as an example of a smart anisotropic biological material, Acta Biomater. 3 (3) (2007) 301–309, https://doi.org/10.1016/j.actbio.2006.10.003.
[15] J. Rivera, et al., Structural design variations in beetle elytra, Adv. Funct. Mater. 31 (50) (Dec. 2021) 2106468, https://doi.org/10.1002/adfm.202106468.
[16] L.E. North, Bioinspired investigation via X-ray microtomography, PhD Swans. Univ. Swans. (2018), https://doi.org/10.23889/Suthesis.43706.
[17] F. Boßelmann, P. Romano, H. Fabritius, D. Raabe, M. Epple, The composition of the exoskeleton of two crustacea: the American lobster Homarus americanus and the edible crab Cancer pagurus, Thermochim. Acta 463 (1–2) (2007) 65–68, https://doi.org/10.1016/j.tca.2007.07.018.
[18] L. Mencattelli, Bio-inspired designs for enhanced damage resistance of composite structures: Bouligand, Herringbone and multi-tailored bone-inspired strategies, p. 170.
[19] N. Suksangpanya, N.A. Yaraghi, R.B. Pipes, D. Kisailus, P. Zavattieri, Crack twisting and toughening strategies in Bouligand architectures, Int. J. Solids Struct. 150 (2018) 83–106, https://doi.org/10.1016/j.ijsolstr.2018.06.004.
[20] S. Yin, et al., Toughening mechanism of coelacanth-fish-inspired double-helicoidal composites, Compos. Sci. Technol. 205 (2021) 108650, https://doi.org/10.1016/j.compscitech.2021.108650.
[21] H.-O. Fabritius, C. Sachs, P.R. Triguero, D. Raabe, Influence of structural principles on the mechanics of a biological fiber-based composite material with hierarchical organization: the exoskeleton of the lobster *Homarus americanus*,", Adv. Mater. 21 (4) (2009) 391–400, https://doi.org/10.1002/adma.200801219.

[22] J. Lian, J. Wang, Microstructure and mechanical anisotropy of crab cancer magister exoskeletons, Exp. Mech. 54 (2) (2014) 229–239, https://doi.org/10.1007/s11340-013-9798-2.
[23] P.-Y. Chen, A.Y.-M. Lin, J. McKittrick, M.A. Meyers, Structure and mechanical properties of crab exoskeletons, Acta Biomater. 4 (3) (2008) 587–596, https://doi.org/10.1016/j.actbio.2007.12.010.
[24] N.A. Yaraghi, et al., A sinusoidally architected helicoidal biocomposite, Adv. Mater. 28 (32) (2016) 6835–6844, https://doi.org/10.1002/adma.201600786.
[25] M. Moini, J. Olek, J.P. Youngblood, B. Magee, P.D. Zavattieri, Additive manufacturing and performance of architectured cement-based materials, Adv. Mater. 30 (43) (2018) 1802123, https://doi.org/10.1002/adma.201802123.
[26] J.L. Liu, E.W.L. Lim, Z.P. Sun, J. Wang, T.E. Tay, V.B.C. Tan, Improving strength and impact resistance of 3D printed components with helicoidal printing direction, Int. J. Impact Eng. 169 (2022) 104320, https://doi.org/10.1016/j.ijimpeng.2022.104320.
[27] R.P. Behera, H.Le Ferrand, Impact-resistant materials inspired by the mantis shrimp's dactyl club, Matter 4 (9) (2021) 2831–2849, https://doi.org/10.1016/j.matt.2021.07.012.
[28] I.M. Van Meerbeek, J.M. Lenhardt, W. Small, T.M. Bryson, E.B. Duoss, T. H. Weisgraber, Compressive properties of silicone Bouligand structures, MRS Bull. 48 (4) (2023) 325–331, https://doi.org/10.1557/s43577-022-00398-z.
[29] J. Liu, S. Li, K. Fox, P. Tran, 3D concrete printing of bioinspired Bouligand structure: a study on impact resistance, Addit. Manuf. 50 (2022) 102544, https://doi.org/10.1016/j.addma.2021.102544.
[30] S.M.F. Kabir, K. Mathur, A.-F.M. Seyam, A critical review on 3D printed continuous fiber-reinforced composites: history, mechanism, materials and properties, Compos. Struct. 232 (2020) 111476, https://doi.org/10.1016/j.compstruct.2019.111476.
[31] C.-C. Tung, Y.-S. Chen, W.-F. Chen, P.-Y. Chen, Bio-inspired, helically oriented tubular structures with tunable deformability and energy absorption performance under compression, Mater. Des. 222 (2022) 111076, https://doi.org/10.1016/j.matdes.2022.111076.
[32] S. Yin, et al., Tough nature-inspired helicoidal composites with printing-induced voids, Cell Rep. Phys. Sci. 1 (7) (2020) 100109, https://doi.org/10.1016/j.xcrp.2020.100109.
[33] O. Keles, A. Karakoc, C.-L. Wu, E.H. Anderson, Enhanced strength, toughness, and reliability in crab exoskeleton inspired additively manufactured porous thermoplastics, Rev. Prepr. (2023), https://doi.org/10.21203/rs.3.rs-2448352/v1.
[34] Z. Li, J. Ma, H. Ma, X. Xu, Properties and applications of basalt fiber and its composites, IOP Conf. Ser. Earth Environ. Sci. 186 (2018) 012052, https://doi.org/10.1088/1755-1315/186/2/012052.
[35] T. Becker, A. Lüking, T. Meinert, S. Panajotovic, J.C.A. Romero, MoonFibre -Fibres from Lunar Regolith (2019), https://doi.org/10.13140/RG.2.2.12287.36007.
[36] I. Cheibas, M. Arnhof, and B. Rich, Basalt fiber composites for the robotic fabrication of a lunar habitat, presented at the 73rd International Astronautical Congress, Paris, Oct. 2022.
[37] N. Coughlin, et al., Development and mechanical properties of basalt fiber-reinforced acrylonitrile butadiene styrene for in-space manufacturing applications, J. Compos. Sci. 3 (3) (2019) 89, https://doi.org/10.3390/jcs3030089.
[38] G. Chabaud, M. Castro, C. Denoual, A. Le Duigou, Hygromechanical properties of 3D printed continuous carbon and glass fibre reinforced polyamide composite for outdoor structural applications, Addit. Manuf. 26 (2019) 94–105, https://doi.org/10.1016/j.addma.2019.01.005.
[39] M. Parker, et al., 3D printing of continuous carbon fiber reinforced polyphenylene sulfide: Exploring printability and importance of fiber volume fraction, Addit. Manuf. 54 (2022) 102763, https://doi.org/10.1016/j.addma.2022.102763.
[40] N. Li, Y. Li, S. Liu, Rapid prototyping of continuous carbon fiber reinforced polylactic acid composites by 3D printing, J. Mater. Process. Technol. 238 (2016) 218–225, https://doi.org/10.1016/j.jmatprotec.2016.07.025.
[41] A. Le Duigou, et al., Thermomechanical performance of continuous carbon fibre composite materials produced by a modified 3D printer, Heliyon 9 (3) (2023) e13581, https://doi.org/10.1016/j.heliyon.2023.e13581.
[42] M.D. Brown, Moisture Absorption and Desorption Effects on Mechanical Behavior in Specialty Polyamide Products, 2019, Accessed: May 25, 2023. [Online]. Available: ⟨https://www.proquest.com/dissertations-theses/moisture-absorption-desorption-effects-on/docview/2384874218/se-2⟩.
[43] R. Matsuzaki, et al., Effects of set curvature and fiber bundle size on the printed radius of curvature by a continuous carbon fiber composite 3D printer, Addit. Manuf. 24 (2018) 93–102, https://doi.org/10.1016/j.addma.2018.09.019.
[44] T. Fruleux, M. Castro, D. Correa, K. Wang, R. Matsuzaki, A.L. Duigou, Geometric limitations of 3D printed continuous flax-fiber reinforced biocomposites cellular lattice structures, Compos. Part C Open Access 9 (2022) 100313, https://doi.org/10.1016/j.jcomc.2022.100313.
[45] J.S. Shang, N.H.H. Ngern, V.B.C. Tan, Crustacean-inspired helicoidal laminates, Compos. Sci. Technol. 128 (2016) 222–232, https://doi.org/10.1016/j.compscitech.2016.04.007.
[46] L. Caetano, B. Galpin, V. Grolleau, J.-D. Capdeville, Behaviour of a birch plywood under various experimental conditions, EPJ Web Conf. 94 (2015) 05010, https://doi.org/10.1051/epjconf/20159405010.
[47] B. Galpin, V. Grolleau, S. Umiastowski, G. Rio, L. Mahéo, Design and application of an instrumented projectile for load measurements during impact, Int. J. Crashworthiness 13 (2) (2008) 139–148, https://doi.org/10.1080/13588260701740634.
[48] Hoberman Collection, Coelacanth. [Online]. Available: ⟨https://animals.howstuffworks.com/endangered-species/coelacanth.htm⟩.
[49] WorldClassPhoto, Mantis Shrimp. 2010. [Picture]. Available: ⟨https://www.shutterstock.com/fr/image-photo/mantis-shrimp-50457778⟩.
[50] Homarus gammarus. [Online]. Available: ⟨https://www.msc.org/be/fr-be/comment-agir/especes-de-poissons-populaires-en-belgique/homard⟩.
[51] W. Ouyang, B. Gong, H. Wang, F. Scarpa, Y. Peng, H.-X. Peng, Identifying the optimal pitch angles for bouligand structures, SSRN J. (2020), https://doi.org/10.2139/ssrn.3677353.
[52] L. An, X. Wu, K. Wang, R. Li, Z. Li, G. Li, Crack modes and toughening strategies of bioinspired 3D printed double-helicoidal architectures, Int. J. Mech. Sci. 253 (2023) 108388, https://doi.org/10.1016/j.ijmecsci.2023.108388.
[53] D. Raabe, C. Sachs, P. Romano, The crustacean exoskeleton as an example of a structurally and mechanically graded biological nanocomposite material, Acta Mater. 53 (15) (2005) 4281–4292, https://doi.org/10.1016/j.actamat.2005.05.027.
[54] R. Desmorat et al., Prévision des endommagements induits par un impact basse vitesse/basse énergie au sein de matériaux composites stratifiés carbone-epoxy de dernière génération.
[55] M.A. Caminero, I. García-Moreno, G.P. Rodríguez, Damage resistance of carbon fibre reinforced epoxy laminates subjected to low velocity impact: effects of laminate thickness and ply-stacking sequence, Polym. Test. 63 (2017) 530–541, https://doi.org/10.1016/j.polymertesting.2017.09.016.
[56] M.K. Hazzard, S. Hallett, P.T. Curtis, L. Iannucci, R.S. Trask, Effect of fibre orientation on the low velocity impact response of thin Dyneema® composite laminates, Int. J. Impact Eng. 100 (2017) 35–45, https://doi.org/10.1016/j.ijimpeng.2016.10.007.
[57] D. Ginzburg, F. Pinto, O. Iervolino, M. Meo, Damage tolerance of bio-inspired helicoidal composites under low velocity impact, Compos. Struct. 161 (2017) 187–203, https://doi.org/10.1016/j.compstruct.2016.10.097.
[58] H. Lv, Low-velocity impact performance of orthogonal grid reinforced CFRP-foam sandwich structure, 2023.
[59] S. Wen, et al., Biomimetic gradient bouligand structure enhances impact resistance of ceramic-polymer composites, Adv. Mater. 35 (21) (2023) 2211175, https://doi.org/10.1002/adma.202211175.
[60] S. Pimenta, R. Gutkin, S.T. Pinho, and P. Robinson, A micromechanical model for kink-band formation: part I — experimental study and numerical modelling, Compos. Sci. Technol., 2009.
[61] L. Mencattelli, S.T. Pinho, Realising bio-inspired impact damage-tolerant thin-ply CFRP Bouligand structures via promoting diffused sub-critical helicoidal damage, Compos. Sci. Technol. 182 (2019) 107684, https://doi.org/10.1016/j.compscitech.2019.107684.
[62] L.K. Grunenfelder, et al., Bio-inspired impact-resistant composites, Acta Biomater. 10 (9) (2014) 3997–4008, https://doi.org/10.1016/j.actbio.2014.03.022.